CrystEngComm

Accepted Manuscript

ROYAL SOCIETY OF CHEMISTRY

www.rsc.org/crystengcomm

Morphology and Lattice Stability Dependent Performance of Nanostructured $Li_4Ti_5O_{12}$ Probed by in situ High-Pressure Raman Spectroscopy and Synchrotron X-ray Diffraction

Fengping Xiao[1], Zhaohui Dong[2], Haiyan Mao[3], Jian Liu[4], Xueliang Sun[4,5] and Yang Song*[,1,5]

[1]Department of Chemistry, The University of Western Ontario, London, Ontario, N6A 5B7, Canada

[2]Shanghai Synchrotron Radiation Facility (SSRF), Shanghai Institute of Applied Physics, CAS, Shanghai, 201204, P. R. China

[3]College of Materials Science and Engineering, Nanjing Forestry University, 159 Longpan Road, Nanjing, Jiangsu, 210037, P. R. China

[4]Department of Mechanical and Materials Engineering, The University of Western Ontario, London, Ontario, N6A 5B9, Canada

[5]Soochow University-Western University Centre for Synchrotron Radiation Research, The University of Western Ontario, London, Ontario, Canada N6A 5B7

*Corresponding author. Email: yang.song@uwo.ca

Abstract

Nanostructured $Li_4Ti_5O_{12}$ (LTO) as a promising anode material in lithium ion battery (LIB) has shown excellent yet morphology-dependent performance in LIB operations. However, the structural origin that influences the material performance at microscopic level remains unclear. Here using combined in situ Raman spectroscopy and synchrotron X-ray diffraction, we comparatively investigated the structural stability of two nanostructured LTO materials with different morphologies by application of external pressure up to 27 GPa. In particular, nanoflower-like $Li_4Ti_5O_{12}$ spheres (LTO-1) and $Li_4Ti_5O_{12}$ nanoparticles (LTO-2) were subject to high pressures using diamond anvil cells and their structural evolutions were characterized upon compression and decompression. Raman measurements show that both LTO materials undergo pressure-induced structural disorder but with different reversibilities upon decompression. X-ray results further confirmed Raman measurements, but also allow the quantitative analysis of pressure dependence of crystal structures. Structural refinements of diffraction patterns yield morphology dependent bulk modulus of the two LTO materials, which reveals critical information about the intrinsic lattice strain and vacancies. These different structural characteristics, when compared with another spinel structure of lithiated titanium dioxide, allows the interpretation of different performance between LTO-1 and LTO-2 for LIB operations. This study thus contributes to the understanding of the important factors that may influence the electrochemical performance and help with the design of new LTO based anode materials for LIB.

1. Introduction

Lithium-ion batteries (LIBs) have been widely used as power sources for electric vehicles because of their high energy density, high power density, and environmentally friendly features.[1-4] However, the technologies of LIBs are currently facing some challenges in safety, cost, and service-life.[5] For instance, carbon materials as anode material suffer from capacity degradation incurred by irreversible side reactions which lead to the formation of solid-electrolyte interphase (SEI) during charge-discharge cycles.[6,7] Thus, better alternative anode materials have been sought after in the past decades. Among all potential candidate materials, lithium titanium oxide ($Li_4Ti_5O_{12}$ or LTO) has attracted much attention due to its uniquely tunable properties as anode materials and thus outstanding performance in LIB operations.[8-14] Compared with other anode materials, the main benefits of $Li_4Ti_5O_{12}$ include no SEI formation and zero lattice strain during lithium intercalation/deintercalation processes.[11] Moreover, $Li_4Ti_5O_{12}$ also has other advantages such as low toxicity, low raw material cost and long cycle life. Compared to the bulk LTO structures, the nanostructured LTO shows significantly improved power capability and reversible capacities.[11] The improvement is believed to be due to the reduction of Li ion diffusion pathway in the particles and better accessibility of the electrolyte to the nanoparticles.[15] As a result, many methods have been developed to synthesize nanostructured LTO. For instance, microwave-assisted hydrothermal (MH) method recently has been successfully applied due to the advantages such as extremely rapid kinetics of crystallization leading to shorter reaction time, as well as mild processing conditions such as lower temperatures required.[16,17]

The crystal structure of $Li_4Ti_5O_{12}$ has been well established as a spinel-type cubic lattice with space group of F$d\bar{3}m$ (Fig. 1). Specifically, the general formula of LTO using Wyckoff notation, can be denoted as $[Li_3]_{8a}[LiTi_5]_{16d}[O_{12}]_{32e}$. All the 8a sites are occupied by lithium and the 16d sites are shared by lithium and titanium with a ratio of 1:5. In the charging process, three moles of Li atoms at 8a sites and three moles of new intercalated Li move to the empty 16c sites. Then, $Li_4Ti_5O_{12}$ converts to a rock salt structure (space group $Fm\bar{3}m$) of $Li_7Ti_5O_{12}$ ($[Li_6]_{16c}[LiTi_5]_{16d}[O_{12}]_{32e}$).[18] The spinel to rock salt phase transition is essential in the understanding of

lithiation/delithiation mechanism and battery performance, and thus has been extensively investigated. Using scanning transmission electron microscopy, for example, Lu et al. probed the nanostructural change of spinel LTO during lithiation and dellithaiation processes and identified significant structure torque that played an important role in the electrochemical performance of LTO.[14] Other possible structual transitions of LTO, such as under high tempeatures, have also been explored.[19] For instance, Leonidov et al.[20] reported a phase transition from spinel structure to a defect structure of the NaCl type due to a redistribution of lithium ions. Overall, new polymorphs of electrode materials observed under non-ambient conditions have attracted recent attentions due to the new structural information with strong implications in the performance of energy devices.[21-23]

In general, the structures and properties of nanomaterials are largely determined by the chemical synthetic routes. However, it has been demonstrated that the application of external pressure can provide an additional driving force to modify the structures as well as morphology of nanomaterials.[24-30] A unique benefit of structural tuning by high pressure study is that pressure-induced phase transformations may provide a new synthetic route for the production of novel structures with improved performance. As a matter of fact, a number of electrode materials have been produced under high pressures with subsequently optimized performance in battery applications.[31-35] Moreover, for electrode materials, structural stability is an important factor which influences the applications of LIBs because structural stability is strongly associated with superior capacity retention and long cycle life. In particular, lattice strain as an important parameter of structural stability and compressibility can be probed and tuned under external compression conditions. In addition, other intrinsic structural characteristics such as lattice defects, interstitials, vacancies, as well as interfacial states, which can be revealed and regulated by compression, may also play important contributing roles in battery performance. For instance, different morphologies of nanostructured LTO materials have been tested with contrasting performance.[17] However, the determining factors associated with the different battery performance

remain unclear. Therefore, studying the structure stability of nanostructured $Li_4Ti_5O_{12}$ and examining the possibility of formation of new structures under external stress, as well as the understanding of the correlation between structures and performance, is of fundamental interest.

Here, we report the first high-pressure study of two different morphologies of nanostructured $Li_4Ti_5O_{12}$ using *in situ* Raman and synchrotron X-ray diffraction techniques. The Raman spectra and X-ray diffraction patterns revealed interesting contrasting high-pressure behaviours between these two nanostructured $Li_4Ti_5O_{12}$ materials, which allow the detailed analysis of structural stability and reversibility. This new structural information at microscopic level provides deep insight into the understanding of battery performance and may provide useful guidance for the design of new anode materials for LIB applications.

2. Experimental

Two different nanostructured $Li_4Ti_5O_{12}$ were synthesized by MH method with a mixture of LiOH, H_2O_2 and titanium tetraisopropoxide (TTIP) following the procedures reported previously.[17] The materials were characterized by X-ray diffraction (XRD, Rigaku RU-200BVH with the Co K-radiation source with λ= 1.7892 Å) and field emission scanning electron microscopy (SEM, Hitachi S4800) to check the crystal structures, purity and the morphology. The SEM images (as shown in Fig. 2) revealed that with different experiment conditions,[17] two morphologies of $Li_4Ti_5O_{12}$ samples were obtained, i.e., nanoflower-like spheres with an average petal thickness of ~10 nm and nanoparticles with size ranging from tens to hundreds of nm) for which we label as LTO-1 and LTO-2, respectively. In a previous electrochemical study, both materials exhibit good discharge capacities but LTO-1 has a better performance in terms of reversibility and cycling lifetime than LTO-2.[17]

A symmetrical diamond anvil cell with two type-I diamonds of 400 μm culets was

used for the high-pressure *in situ* Raman measurements and synchrotron X-ray diffraction experiment. A hole with a diameter of 130 μm was drilled at the centre of the stainless steel gasket and used as a sample chamber. The samples were loaded without pressure transmitting medium (PTM) for Raman measurements, whereas silicon oil was used as the PTM for X-ray diffraction measurements. A few ruby chips were inserted into the sample chamber as the pressure calibrant before loading the LTO samples and pressure was determined by the well-established ruby fluorescence method.

In situ high-pressure Raman spectroscopy was performed using a customized Raman system in house. Briefly, A 782 nm solid state laser with an output power of 50 mW was used as the excitation source. The scattered light was then dispersed using an imaging spectrograph (SpectroPro-2500i, Acton Research Corporation) equipped with a 1200 lines/mm grating achieving a 0.1 cm^{-1} resolution. The Raman signal was recorded using an ultrasensitive, liquid nitrogen cooled, back-illuminated, charge-coupled device (CCD) detector from Acton. The Rayleigh scattering was removed by an edge filter. The system was calibrated by neon lines with an uncertainty of ± 1 cm^{-1}. Raman spectra for each pressure point were collected with an accumulation time of 200 s in the spectral region of 100-800 cm^{-1}, corresponding to the lattice vibrations.

Angle-dispersive X-ray diffraction measurements on both LTO samples were carried out on compression and decompression at pressures up to 27 GPa and reproduced at two different synchrotron facilities, i.e., Shanghai Synchrotron Radiation Facility (SSRF), China and Advanced Photon Source (APS) in Argonne National Laboratory (ANL), USA. Specifically, a hard X-ray micro-focusing undulator beamline, BL15U1 at SSRF equipped with Si (111) double crystal monochromator producing λ=0.6888 Å X-ray beam was used for *in-situ* diffraction experiments. The beam size at the sample was estimated to be 10 μm in diameter. The diffraction data were recorded on

a MAR-165 CCD detector with an exposure time of 60 s. Similar diffraction measurements were also carried out at beamline 16BM-D at APS. The radiation with λ=0.4246 Å and with a comparable beam size of 5 × 12 μm^2 was used and the diffraction data were recorded on a MAR345 imaging plate with an exposure time of 60 s. CeO_2 was used as calibration material at both beamlines. The 2D Debye-Scherrer diffraction patterns were integrated by using Fit2D program for further analysis. The structural refinement was performed using GSAS software package.

3. Results and discussion

Selected Raman spectra of LTO-1 and LTO-2 collected upon compression up to ~24 GPa followed by decompression to ambient were shown in Figure 3 and 4, respectively. Five active Raman modes were predicted for spinel structure of $Li_4Ti_5O_{12}$: $A_{1g} + E_g + 3F_{2g}$.[20] For LTO-1 sample, three major modes corresponding to $F_{2g,}$ E_g and $A_{1g,}$ are observed at 222, 425, and 665 cm^{-1} respectively at near ambient condition. This observation agrees with that from Knyazev et al.[19] (235, 429, and 675 cm^{-1}) and that from Aldon et al.[36] (246, 429 and 680 cm^{-1}) reasonably well. The F_{2g} mode at 222 cm^{-1} predominantly related to oxygen atom displacement but involve also lithium ion motions, especially in the low frequency region of the spectra.[19] The E_g mode at 425 cm^{-1} can be assigned to the stretching motion of the Li-O ionic bonds located in LiO_4 tetrahedral (E_g).[36] The highest frequency mode of A_{1g} at 665 cm^{-1} originates from the stretching motion of Ti-O covalent bonding in TiO_6 octahedra.[37] The corresponding frequencies of these three modes for LTO-2 were observed at 248, 451 and 687 cm^{-1} respectively. In addition, another F_{2g} mode at 347 cm^{-1} also corresponding to the Li-O stretching motion was observed for LTO-2 sample, consistent with that by Knyazev et al. and Aldon et al. (i.e., 347 and 360 cm^{-1}, respectively). Moreover, additional minor peaks for LTO-1 (e.g., 331, 388 and 509 cm^{-1}), and LTO-2 (e.g., 310, 326, and 392 cm^{-1}) were also observed. The different

number of Raman modes as well as the different frequencies of Raman modes between the two LTO samples and previous references is most likely associated with morphology effect and detailed local lattice structures. It has been suggested that the number of lattice modes is often inconsistent with the Raman or IR selection rules for spinel structures. For instance, the additional bands observed may be originated from the disorder effects.[19] In the case of LTO-2, in particular, the additional Raman bands observed may indicate combined disorder effect and defect in the crystal lattice. The high-quality X-ray diffraction patterns collected at ambient pressure can clearly rule out the impurity in either LTO samples.

Upon compression to 15.5 GPa stepwise, all Raman bands of LTO-1 shift to higher frequencies with decreasing intensity and band broadening (Fig. 3). At the highest pressure of ~23.4 GPa, all Raman bands mostly vanished. These observations suggest gradual pressure-induced disordering and possibly to an amorphous state without well-defined crystalline-to-crystalline transitions. Similar trends were observed for LTO-2 (Fig. 4) except that the F_{2g} mode at 248 cm^{-1} was substantially depleted when compressed to 4.8 GPa. In addition, the minor Raman bands in the region of 300-425 cm^{-1} are also significantly weakened at 10.8 GPa and above, leaving only the major characteristic lattice modes (i.e., F_{2g}, E_g and A_{1g}) observed. The pressure behaviors of all these modes, which are associated with Li-O stretching vibrations, suggest instability of Li-O lattice possibly due to the lattice defect in LTO-2. LTO-2 was also found to go to a disordered or an amorphous state at similar pressure above 20 GPa as indicated by broadened featureless Raman profile.

The reversibility of pressure effect on crystal structures provides important information on transformation mechanism. Therefore, Raman spectra were also collected upon decompression to near ambient pressure for both samples. Gradual back transformation from disordered to crystalline structures was observed as indicated by the recovery of major Raman bands for both samples. However, the

recovered LTO-1 Raman spectrum show highly similar profile to that before compression with three major bands clearly resolved, whereas the minor bands in the region of 300-425 cm^{-1} for LTO-2 were not recovered. This observation suggests the reversibility of pressure-induced structural disordering of LTO-1 is significantly higher than LTO-2. Since all non-recovered bands in LTO-2 are believed to be associated with vibrations of disordered Li-O tetrahedrons, clearly these defect sites do not sustain external stress at this level and thus have been substantially modified by compression.

Selected diffraction patterns for LTO-1 collected upon compression to 27.1 GPa followed by decompression are depicted in Fig. 5. The diffraction patterns and pressure sequence for LTO-2 are very similar to LTO-1 and thus only the patterns at highest comparable pressure and of recovered LTO-2 were plotted. All the four major reflections observed at the near ambient pressure can be well indexed to a spinel-type structure. By structural refinement, the unit cell parameters a = 8.2666 Å and 8.3071 Å were obtained for LTO-1 and LTO-2 respectively, consistent with the value of $Li_4Ti_5O_{12}$ reference materials (JCPDS No. 49-0207).[38] Upon compression, all the reflections of shifted to higher 2θ angle monotonically, indicating a pressure-induced reduction of d-spacing and thus the unit cell volume, but without phase transitions. With increasing pressure, the reflections become generally broadened and weakened, such that only the primary reflection of (111) can be observed at highest pressure of 27 GPa. These observations suggest that LTO-1 maintains its crystal structure but with reduced crystallinity. In contrast, even at 26.3 GPa, LTO-2 exhibited extremely weakened diffraction intensity (Fig. 5) suggesting substantial disorderness or even the amorphization of the crystal lattice, consistent with the Raman measurements. When the pressure was released to near ambient, all three diffraction peaks of LTO-1 are observed again which suggests pressure induced structural modifications is mostly reversible. The structural refinement yielded a slightly modified unit cell parameter of a = 8.2711 Å for LTO-1, whereas the extremely weak reflection intensity of the

recovered LTO-2 (Fig. 5) does not allow the unambiguous refinement of the cell parameter, suggesting that pressure-induced disordering in LTO-2 is mostly irreversible.

In addition to the structural reversibility characterized by Raman spectroscopy and X-ray diffraction, the morphology changes of LTO-1 and LTO-2 upon compression and decompression were also characterized by SEM (Fig. 2c and 2d). The SEM images show that morphology of nanoflower-like $Li_4Ti_5O_{12}$ (LTO-1) exhibited a dramatic change such that the original flower-like morphology is no longer recognizable in the recovered sample. In contrast, the nanoparticle morphology of LTO-2 is still recognizable after the compression-decompression cycle. This observation together with the larger bulk modulus (discussed below) implies the higher toughness of the $Li_4Ti_5O_{12}$ nanoparticles (i.e., LTO-2).

The evolution of the lattice parameter and unit cell volume of both LTO-1 and LTO-2 samples with pressure were obtained from the structural refinement of the diffraction patterns. Figures 6 and 7 show the comparative pressure-dependent variations of relative lattice parameters between LTO-1 and LTO-2, and normalized unite cell volumes as a function of pressure, respectively. As shown in Fig. 6, both LTO materials with isotropic cubic structure exhibit monotonic compression behavior, however, with LTO-1 having larger compressibility than LTO-2. The pressure-volume data of LTO-1 and LTO-2 were fitted to third order Birch-Murnaghan equation of state (EOS):

$$P/B_0 = 3/2\left(x^{7/3} - x^{5/3}\right)\left[1 + 3/4(B_0' - 4)\left(x^{2/3} - 1\right)\right]$$

where $x = V_0/V$, the ratio of zero-pressure volume over the volume at pressure P. The constants B_0 and B_0' are the isothermal bulk modulus and its pressure derivative, respectively. The EOS for LTO-1 and LTO-2 upon compression are shown in Fig. 7.

The bulk moduli (B_0) of these two LTO samples were determined to be 123 GPa (LTO-1) and 167 GPa (LTO-2), respectively, when $B_0^{'}$ is fixed at 4. Evidently, both the unit cell parameters and EOS suggest that nanoflower-like $Li_4Ti_5O_{12}$ spheres are more compressible than $Li_4Ti_5O_{12}$ nanoparticles. The morphology dependent variation of bulk modulus has been reported in other high-pressure studies of nanomaterials before.[24,26,30] It is the general understanding that the surface energy associated with different nanostructures may play a major role in influencing the compressibility of the materials. In particular, reduced dimensions and enhanced surface areas may results in the elevation of bulk modulus, such as observed in TiO_2,[24] SnO_2,[26] and ZnO,[30] etc., which all exhibit larger bulk modulus (i.e., lower compressibility) than the corresponding bulk materials. Therefore, we can speculate that the bulk modulus of bulk LTO materials will be lower compared to nanostructured LTO materials in the current study.

Prior to the current high-pressure study, it has been reported that nanostructured LTO has an improved performance than bulk materials in the LIB applications.[11] Moreover, LTO-1 shows a substantially higher discharge capacity than LTO-2.[17] Thus it is of fundamental interest to understand the origin of the difference and correlation between the performance in LIB operations and their high-pressure behaviors of the two morphologies of LTO materials. As mentioned before, the lattice strain plays an important role during lithium intercalation/deintercalation processes.[5] The lattice strain, however, may be altered substantially as a function of grain size and morphology. Ouyang et al.[39] recently proposed the atomistic origin of the lattice strain in nanostructured materials. In particular, it was found that the lattice strain has a positive correlation with bulk modulus, i.e., larger lattice strain with increasing bulk modulus. Based on this relationship, we can infer that LTO-2 as nanoparticles has a larger intrinsic lattice strain than that of LTO-1 as nanoflower-like spheres, consistent with the observation of the better performance of LTO-1 in LIB operations. We note that reduced dimension such as from bulk to nanostructures often includes larger

lattice stain, which is unfavorable for the lithium intercalation/deintercalation.[11] However, the enhanced surface area of the nanostructures which facilitates Li^+ diffusion and exchange outweighs the negative impact of lattice strain in LTO-1, whereas in LTO-2, lattice strain is likely a dominant factor for the performance in the LIB operations.

In addition, Xiong et al.[21] proposed that the lattice stability may have strong influence on the long-term operation of Li-ion batteries. In their recent high-pressure study of lithiated cubic titania (c-TiO_2) nanotube with compositional variations for $Li_x(TiO_2)$ where x ranges from 0 and 1, a vacancy filling mechanism was invoked to interpret the structural stability by means of application of applied pressure that drives the interstitial Li^+ to the cation vacancy of oxide polyhedrons. Specially, it was found that pure c-TiO_2 (with the same spinel structure as $Li_4Ti_5O_{12}$) undergoes a pressure induced amorphization at only 17.5 GPa, whereas lithiated TiO_2 structures with liathiation ratio of 0.5, 0.75 and 1.0 all sustained high compression and remained crystalline at pressures even over 50 GPa. The molecular dynamic simulations further reveals that the 75% lithiated cubic TiO_2 (a unique lithium concentration) exists in a two-phase mixture of crystalline and amorphous phase at high pressures > 35 GPa. Our results of LTO-1 are in excellent agreement with that of Xiong's in that 1) $Li_4Ti_5O_{12}$ can be considered a liathiation ratio of 4/5 or 80%, close to 75% lithiated cubic TiO_2; and that 2) LTO-1 also remains crystalline at the highest pressure, but with pressure-induced disordering and partial reversibility upon decompression. Moreover, the slightly lower bulk modulus for 75% lithiated cubic TiO_2 (i.e., ～100 GPa) in excellent alignment with those for LTO-1 and LTO-2 obtained in this study. The relative order of the compressibility, i.e., ($Li_{0.75}TiO_2$> LTO-1> LTO-2 as shown in Fig. 7) also suggests the same order of available lattice vacancy that allows additional Li ion intake and occupation of the interstitial sites by diffusion, an essential process for LIB operation. Although having the same Li/Ti ratio as LTO-1, the lattice defect and intrinsic local disorder of LTO-2, on the other hand, shows a

poor structural stability and reversibility. These analyses not only account for the better performance and durability of LTO-1 than LTO-2, but allows extrapolation that lithiatiated c-TiO_2 could be made into a slightly improved anode material with performance even better than LTO-1. Overall, this study has established an important guideline that the combination of multiple factors including the surface area, lattice strain, local defect and disorderness, available vacancies, and ultimately the lattice stability must be considered as an important input in the design of new nanostructured electrode materials in the future.

4. Conclusions

In summary, two different morphologies of nanostructured $Li_4Ti_5O_{12}$ materials, i.e., nanoflower-like sphere (LTO-1) and nanoparticles (LTO-2) were investigated under high pressure using *in situ* Raman spectroscopy and synchrotron X-ray diffraction. No phase transformations other than pressure-induced structural disordering were observed in both samples. Both the Raman and diffraction measurements suggest that reversibility of the structural changes of LTO-1 is substantially higher than LTO-2. Structural refinement of the diffraction patterns allows the analysis of equation of states of both materials by yielding the respective bulk modulus of 123 GPa and 167 GPa, indicating morphology dependent compressibilities of nanostructured $Li_4Ti_5O_{12}$. Moreover, the higher compressibility of LTO-1 than LTO-2 was examined in comparison with other nanostructured lithium titanium dioxide. The difference in compressibility and reversibility suggest different lattice vacancies and structural stabilities between the two different LTO nanostructures. Based on the positive correlation between lattice strains with bulk modulus, it can be inferred that LTO-2 has a larger intrinsic lattice strain than that of LTO-1. All these analysis consistently interpret the observation of the better performance of LTO-1 that LTO-2 in LIB operations reported previously. Our study thus contributes to the design of new nanostructured anode materials by providing a practical guideline by considering

multiple combined factors that may influence that their performance in the LIB operations.

Acknowledgments

This work was supported by a Discovery Grant, a Research Tools and Instruments Grant from the Natural Science and Engineering Research Council of Canada, a Leaders Opportunity Fund from the Canadian Foundation for Innovation, an Early Researcher Award from the Ontario Ministry of Research and Innovation, a Petro-Canada Young Innovator Award. We acknowledge Dr. D. Popov for his technical assistance for the X-ray diffraction experiments. This work was partially performed at BL15U1 at Shanghai Synchrotron Radiation Facility (SSRF), China, and partially at HPCAT (Sector 16), Advanced Photon Source (APS), Argonne National Laboratory under the support from Carnegie DOE Alliance Center (CDAC). HPCAT operations are supported by DOE-NNSA under Award No. DE-NA0001974 and DOE-BES under Award No. DE-FG02-99ER45775, with partial instrumentation funding by NSF.

Reference

(1) Armand, M.; Tarascon, J. M. *Nature*, 2008, **451**, 652.
(2) Tarascon, J. M.; Armand, M. *Nature*, 2001, **414**, 359.
(3) Kang, K. S.; Meng, Y. S.; Breger, J.; Grey, C. P.; Ceder, G. *Science*, 2006, **311**, 977.
(4) Winter, M.; Besenhard, J. O.; Spahr, M. E.; Novak, P. *Adv. Mater.*, 1998, **10**, 725.
(5) Etacheri, V.; Marom, R.; Elazari, R.; Salitra, G.; Aurbach, D. *Energy Environ. Sci.*, 2011, **4**, 3243.
(6) Kaskhedikar, N. A.; Maier, J. *Adv. Mater.*, 2009, **21**, 2664.
(7) Arora, P.; White, R. E.; Doyle, M. *J. Electrochem. Soc.*, 1998, **145**, 3647.
(8) Ferg, E.; Gummow, R. J.; Dekock, A.; Thackeray, M. M. *J. Electrochem. Soc.*, 1994, **141**, L147.
(9) Zaghib, K.; Armand, M.; Gauthier, M. *J. Electrochem. Soc.*, 1998, **145**, 3135.
(10) Liu, P.; Sherman, E.; Verbrugge, M. *J. Solid State Electrochem.*, 2010, **14**, 585.
(11) Yi, T. F.; Yang, S. Y.; Xie, Y. *J. Mater. Chem. A*, 2015, **3**, 5750.

(12) Wu, N.; Yang, Z. Z.; Yao, H. R.; Yin, Y. X.; Gu, L.; Guo, Y. G. *Angew. Chem.-Int. Edit.*, 2015, **54**, 5757.
(13) Haridas, A. K.; Sharma, C. S.; Rao, T. N. *Small*, 2015, **11**, 290.
(14) Lu, X.; Gu, L.; Hu, Y. S.; Chiu, H. C.; Li, H.; Demopoulos, G. P.; Chen, L. Q. *J. Am. Chem. Soc.*, 2015, **137**, 1581.
(15) Amine, K.; Belharouak, I.; Chen, Z. H.; Tran, T.; Yumoto, H.; Ota, N.; Myung, S. T.; Sun, Y. K. *Adv. Mater.*, 2010, **22**, 3052.
(16) Komarneni, S.; Rajha, R. K.; Katsuki, H. *Mater. Chem. Phys.*, 1999, **61**, 50.
(17) Liu, J.; Li, X. F.; Yang, J. L.; Geng, D. S.; Li, Y. L.; Wang, D. N.; Li, R. Y.; Sun, X. L.; Cai, M.; Verbrugge, M. W. *Electrochim. Acta*, 2012, **63**, 100.
(18) Schmidt, W.; Bottke, P.; Sternad, M.; Gollob, P.; Hennige, V.; Wilkening, M. *Chem. Mat.*, 2015, **27**, 1740.
(19) Knyazev, A. V.; Smirnova, N. N.; Maczka, M.; Knyazeva, S. S.; Letyanina, I. A. *Thermochimica Acta*, 2013, **559**, 40.
(20) Leonidov, I. A.; Leonidova, O. N.; Perelyaeva, L. A.; Samigullina, R. F.; Kovyazina, S. A.; Patrakeev, M. V. *Phys. Solid State*, 2003, **45**, 2183.
(21) Xiong, H.; Yildirim, H.; Podsiadlo, P.; Zhang, J.; Prakapenka, V. B.; Greeley, J. P.; Shevchenko, E. V.; Zhuravlev, K. K.; Tkachev, S.; Sankaranarayanan, S.; Rajh, T. *Phys. Rev. Lett.*, 2013, **110**, 078304.
(22) Wang, Y. H.; Lu, X. J.; Yang, W. G.; Wen, T.; Yang, L. X.; Ren, X. T.; Wang, L.; Lin, Z. S.; Zhao, Y. S. *J. Am. Chem. Soc.*, 2015, **137**, 11144.
(23) Lin, Y.; Yang, Y.; Ma, H. W.; Cui, Y.; Mao, W. L. *J. Phys. Chem. C*, 2011, **115**, 9844.
(24) Dong, Z. H.; Song, Y. *Can. J. Chem.*, 2015, **93**, 165.
(25) Dong, Z. H.; Song, Y. *Appl. Phys. Lett.*, 2010, **96**, 151903.
(26) Dong, Z. H.; Song, Y. *Chem. Phys. Lett.*, 2009, **480**, 90.
(27) San-Miguel, A. *Chem. Soc. Rev.*, 2006, **35**, 876.
(28) Lu, X. J.; Yang, W. G.; Quan, Z. W.; Lin, T. Q.; Bai, L. G.; Wang, L.; Huang, F. Q.; Zhao, Y. S. *J. Am. Chem. Soc.*, 2014, **136**, 419.
(29) Dong, Z. H.; Song, Y. *J. Phys. Chem. C*, 2010, **114**, 1782.
(30) Dong, Z. H.; Zhuravlev, K. K.; Morin, S. A.; Li, L. S.; Jin, S.; Song, Y. *J. Phys. Chem. C*, 2012, **116**, 2102.
(31) Fell, C. R.; Lee, D. H.; Meng, Y. S.; Gallardo-Amores, J. M.; Moran, E.; Arroyo-de Dompablo, M. E. *Energy Environ. Sci.*, 2012, **5**, 6214.
(32) Yoncheva, M.; Stoyanova, R.; Zhecheva, E.; Alcantara, R.; Ortiz, G.; Tirado, J. L. *J. Solid State Chem.*, 2007, **180**, 1816.
(33) Gallardo-Amores, J. M.; Biskup, N.; Amador, U.; Persson, K.; Ceder, G.; Moran, E.; Arroyo, M. E.; de Dompablo, M. *Chem. Mat.*, 2007, **19**, 5262.
(34) Garcia-Moreno, O.; Alvarez-Vega, M.; Garcia-Alvarado, F.; Garcia-Jaca, J.; Gallardo-Amores, J. M.; Sanjuan, M. L.; Amador, U. *Chem. Mat.*, 2001, **13**, 1570.
(35) Voss, B.; Nordmann, J.; Kockmann, A.; Piezonka, J.; Haase, M.; Taffa, D. H.; Walder, L. *Chem. Mat.*, 2012, **24**, 633.

(36) Aldon, L.; Kubiak, P.; Womes, M.; Jumas, J. C.; Olivier-Fourcade, J.; Tirado, J. L.; Corredor, J. I.; Vicente, C. P. *Chem. Mat.*, 2004, **16**, 5721.
(37) Kellerman, D. G.; Gorshkov, V. S.; Shalaeva, E. V.; Tsaryev, B. A.; Vovkotrub, E. G. *Solid State Sci.*, 2012, **14**, 72.
(38) Fang, W.; Ma, Y. L.; Zuo, P. J.; Cheng, X. Q.; Yin, G. P. *Int. J. Electrochem. Sci.*, 2013, **8**, 1949.
(39) Ouyang, G.; Zhu, W. G.; Sun, C. Q.; Zhu, Z. M.; Liao, S. Z. *Phys. Chem. Chem. Phys.*, 2010, **12**, 1543.

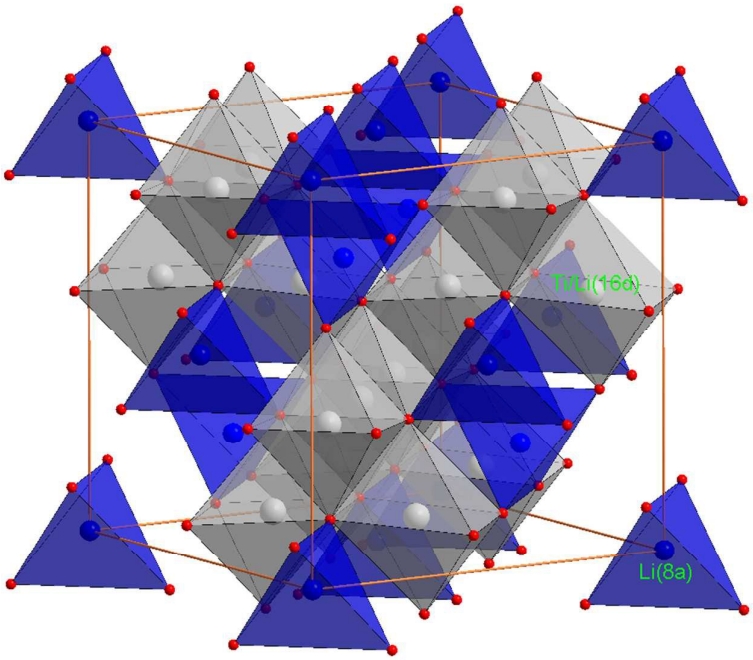

Fig. 1. Crystal structure of spinel-type $Li_4Ti_5O_{12}$ (space group $Fd\bar{3}m$) at ambient conditions. Li (blue and grey spheres) occupies 16d and 8a sites; Ti (grey spheres) occupies 16 site; Oxygen (red spheres) occupies 32a site.

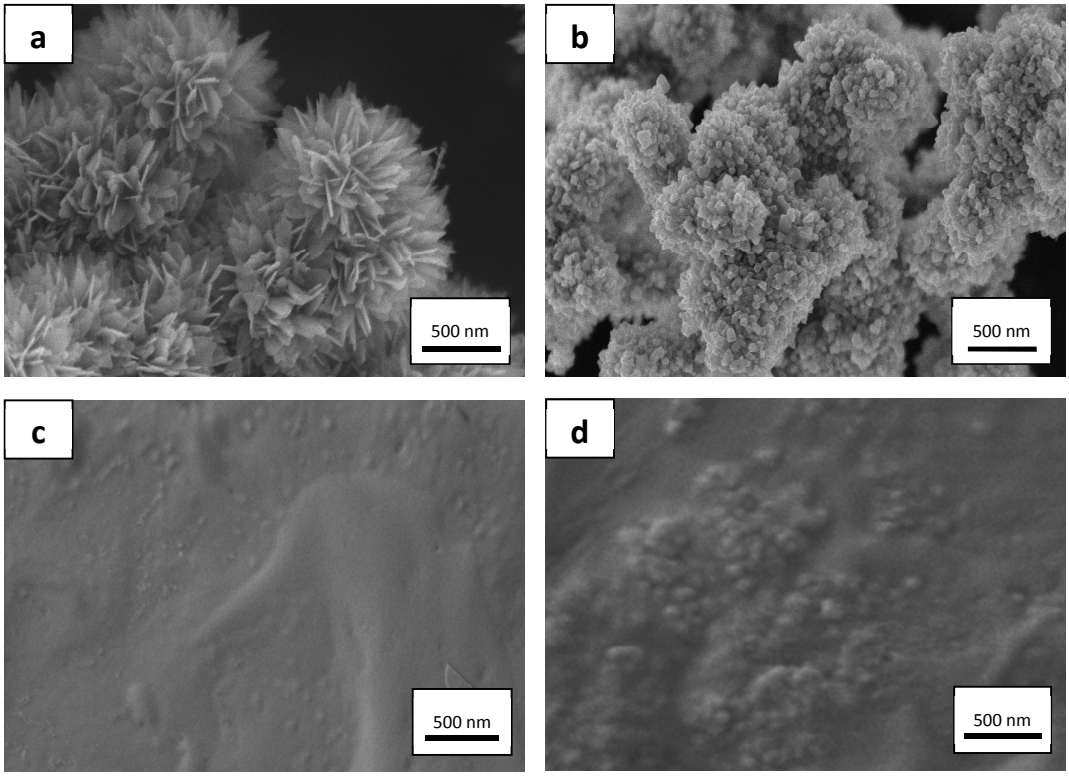

Fig. 2. SEM images of nanoflower-like $Li_4Ti_5O_{12}$ spheres (LTO-1) (a) and $Li_4Ti_5O_{12}$ (LTO-2) nanoparticles (b) as starting materials before compression in comparison with those after compression/decompression, (c) and (d), respectively.

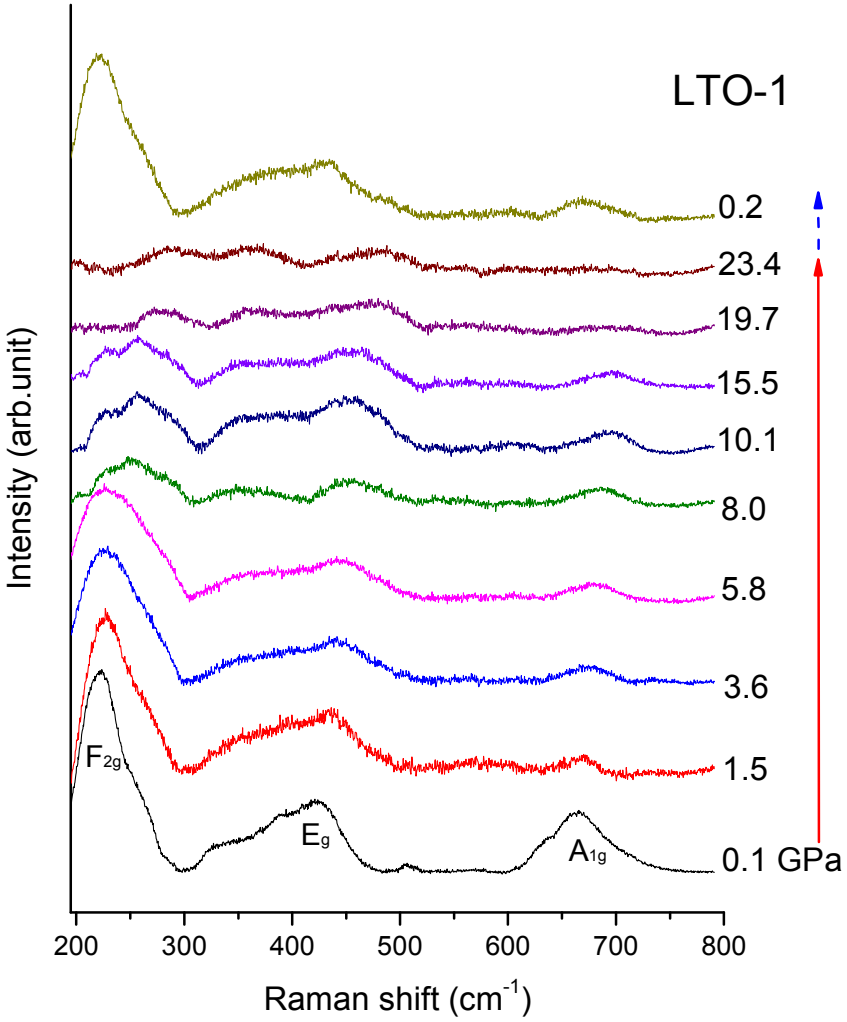

Fig. 3. Selected Raman spectra of LTO-1 upon compression and decompression. The red and blue arrows indicate the compression and decompression sequence, respectively.

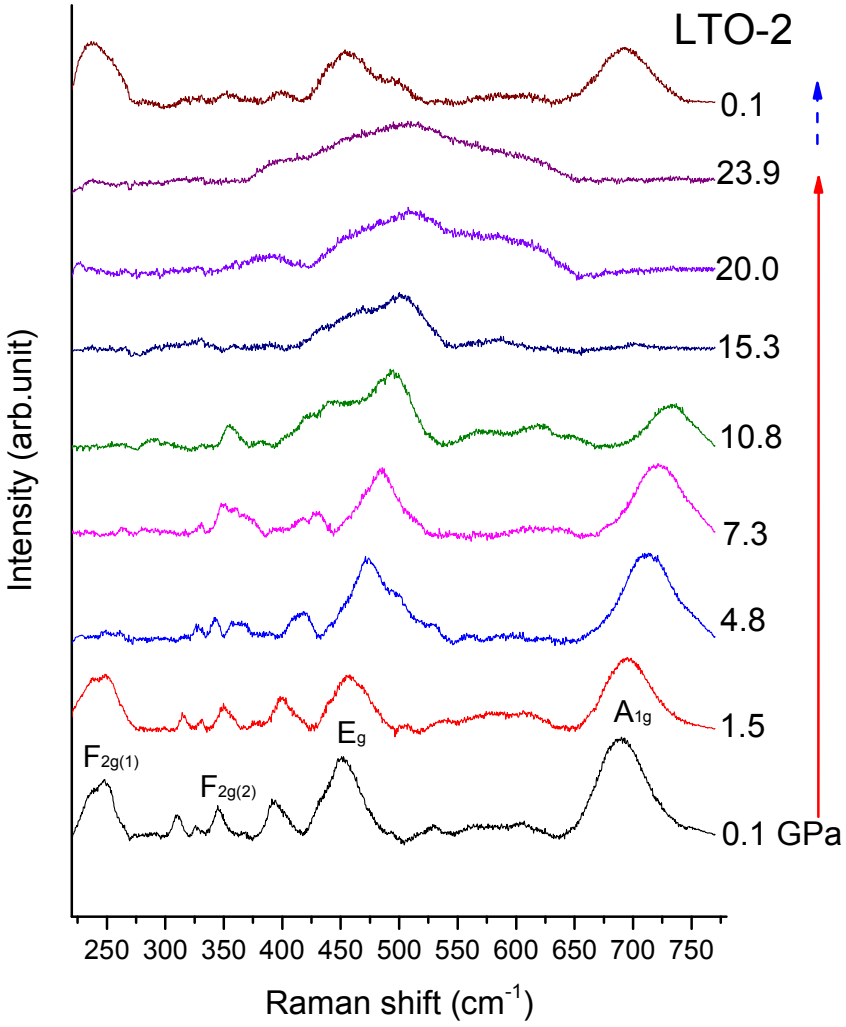

Fig. 4. Selected Raman spectra of LTO-2 upon compression and decompression. The red and blue arrows indicate the compression and decompression sequence, respectively.

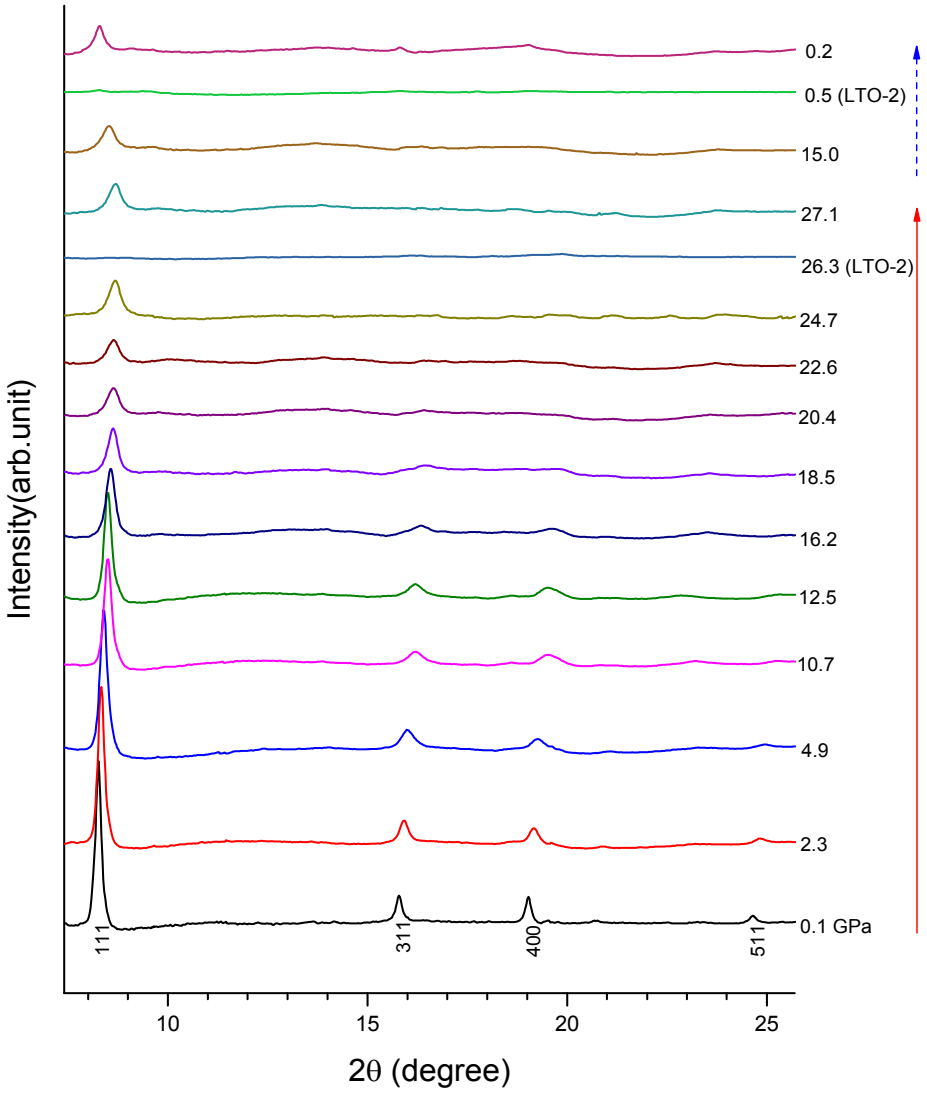

Fig. 5. X-ray diffraction patterns (λ=0.6888 Å) for LTO-1 upon compression and decompression at selected pressures. The red and blue arrows indicate the compression and decompression sequence, respectively. The diffraction patterns for LTO-2 at upon compression to highest pressure of 26.3 GPa and decompression to near ambient pressure are also plotted below the LTO-1 patterns at the corresponding pressures for comparison purposes.

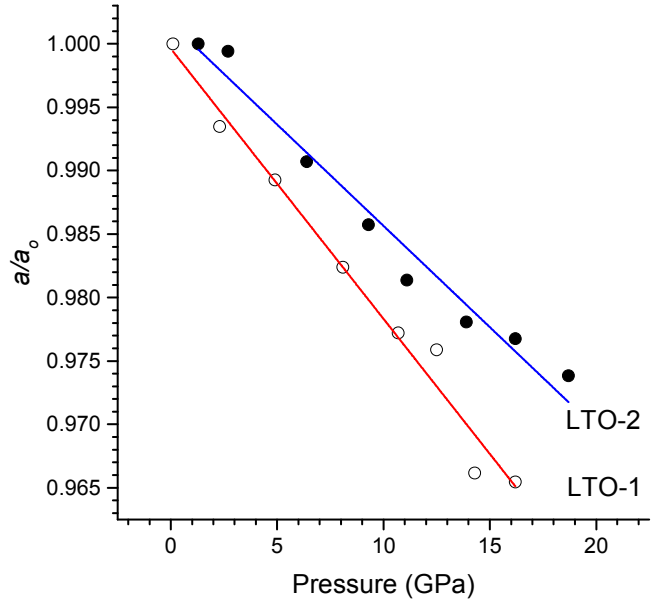

Fig. 6. Cell parameter ratio (a/a_0) as a function of pressure for LTO-1 (open circle) and LTO-2 (solid circle). Solid lines are for eye guidance only.

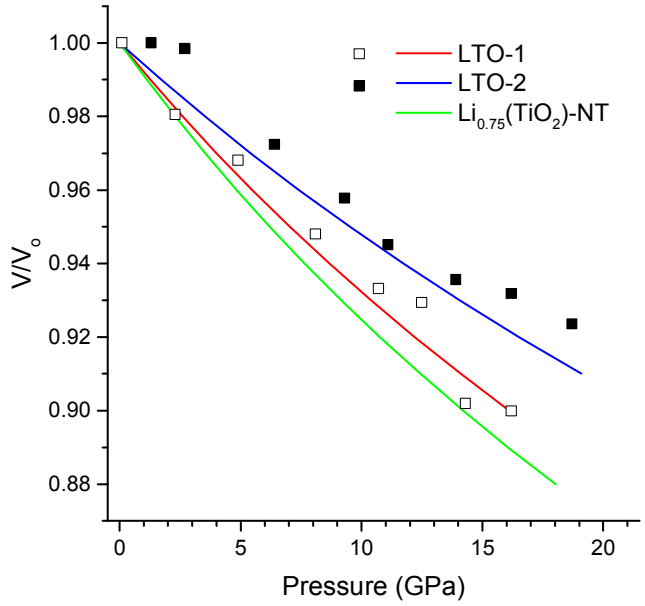

Fig. 7. Normalized unit cell volume (V/V_0) as a function of pressure derived from structural refinement of X-ray diffraction patterns for LTO-1 (open square) and LTO-2 (solid square), and the corresponding equation of state (red and blue solid lines, respectively).The green solid line denotes the equation of state for $Li_{0.75}(TiO_2)$ nanotubes derived from Ref. 21.

TOC Graphic

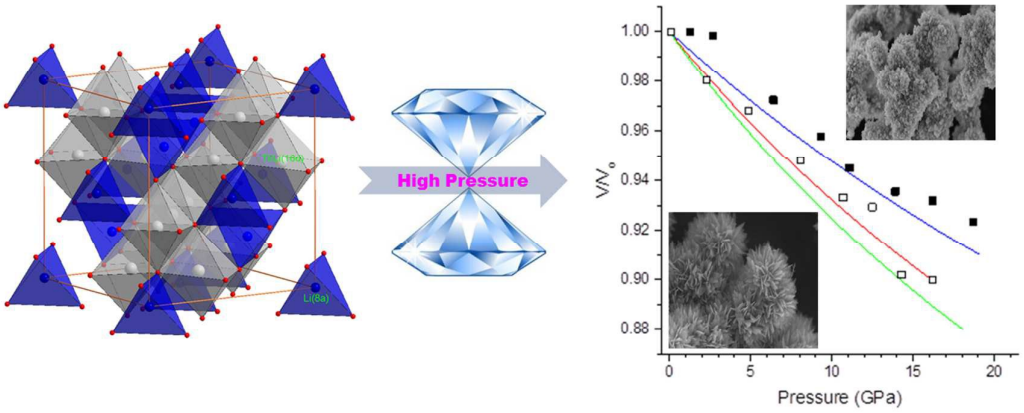

In situ high-pressure measurements of two different nanostructured $Li_4Ti_5O_{12}$ materials revealed important structural origins that influence the electrochemical performance.